Morphology Transition from Cylindrical to Lamellar Microdomains of Block Copolymers

Shinichi Sakurai,* Toshikazu Momii, Kazuhiro Taie, Mitsuhiro Shibayama, and Shunji Nomura

Department of Polymer Science and Engineering, Kyoto Institute of Technology, Matsugasaki, Sakyo-ku, Kyoto 606, Japan

Takeji Hashimoto

Department of Polymer Chemistry, Kyoto University, Sakyo-ku, Kyoto 606-01, Japan

Received August 4, 1992; Revised Manuscript Received October 6, 1992

ABSTRACT: Thermally induced morphology transition from cylindrical to lamellar microdomains was found for a poly(styrene-*block*-butadiene-*block*-styrene) (SBS) triblock copolymer having a 0.56 weight fraction of polystyrene blocks by small-angle X-ray scattering (SAXS) and transmission electron microscopy (TEM). Polybutadiene (PB) cylinders with hexagonal close packing were formed in a polystyrene (PS) matrix when the SBS was cast from a methyl ethyl ketone solution. It was found that the PB cylinders were transformed into lamellae on annealing at 150 °C. This is a transition from thermodynamically quasi-stable to stable morphologies. On the basis of SAXS and TEM, the transition turned out to occur via coalescence of cylinders without their translational movements. It is proposed that an undulation of the interface induced by the instability of the interface might play an important role for the coalescence of the cylinders. It was also found by TEM that the coherency of lamellar microdomains thus formed became higher with further annealing; i.e., the persistence length of the undulating lamellae became longer.

I. Introduction

In multiphase polymeric systems morphology control is one of the most important research subjects, since their mechanical properties depend strongly on their structures.[1] In the case of block copolymers it is possible to design multiphase domain structures of submicron (mesoscopic) scale via microphase separation[2] so as to obtain desired properties. A–B type block copolymers in melts may form microdomains due to strong segregation between the A and B block chains, and their morphologies are determined primarily by composition of a block copolymer. Molau[3] has presented five fundamental morphologies, i.e., A (B) spheres in a B (A) matrix, A (B) cylinders in a B (A) matrix, and alternating lamellae. We have investigated systematically the microdomain structures of block copolymers by small-angle X-ray scattering (SAXS) and transmission electron microscopy (TEM) and have obtained various results on the morphology, domain size, their dependencies of molecular weight and composition, and so forth.[4–7]

Meier[8,9] and Helfand et al.[10–14] have developed statistical thermodynamical theories for microdomain structures of block copolymers. According to these theories, it is possible to expect equilibrium domain sizes for respective morphologies (e.g., spheres, cylinders, and lamellae) with a given set of molecular weight and composition. These theories allow us to predict also equilibrium morphology in a strong segregation limit. Hong, Noolandi, Whitmore, and their co-workers have presented a functional integral theory for copolymer/solvents blends[15–17] and copolymer/homopolymer mixtures.[16–18] The functional integral theory which is a self-consistent theory makes no a-priori assumptions of weak or strong segregation limits. Leibler[19] has developed a Landau type *mean-field* theory on the microphase-separation transition (MST) in block copolymers and has presented the phase diagram for the microdomain morphologies in the weak-segregation limits as a function of segregation power and composition of the block copolymer. Recently Ohta and Kawasaki[20] have generalized Leibler's theory to the strong-segregation limit by taking into account a long-range interaction of the local order parameter on the basis of the Ginzburg–Landau type *mean-field* theory. More recently Fredrickson and Helfand[21] have corrected Leibler's *mean-field* theory to take into account the effect of composition fluctuations on the MST. These theories expect that the morphologies are changed with the segregation power. Since the segregation power is a function of temperature, morphology may be reversibly controlled and hence the transition between the different kinds of morphologies may occur by changing temperature. However, this kind of thermally reversible transition has not been experimentally confirmed up to the present, except in our recent preliminary results.[22]

Another possible way to control the morphology is an application of thermally induced irreversible morphological transition.[23,24] As for the irreversible transition, it was experimentally confirmed that lamellar microdomains which were formed in the solution-cast films with a selective solvent were transformed into cylindrical microdomains by annealing above the glass transition temperature, T_g.[23] In this case, it was considered that a thermodynamically quasi-stable lamellar morphology, which was frozen due to vitrification during solvent evaporation, was changed to a stable cylindrical morphology upon annealing above T_g. In this paper we present a similar irreversible but inverse morphology transition from cylindrical to lamellar microdomains as observed by SAXS and confirmed by TEM. Since the mechanism of forming quasi-stable morphology with a selective cast-solvent was a scope of the previous work,[23] we exclusively focus here on a mechanism of the morphology transition from cylindrical to lamellar microdomains, elucidation of which may give a new aspect for morphology control.

II. Experimental Section

A poly(styrene-*block*-butadiene-*block*-styrene) triblock copolymer coded as TR2400 (the commercial sample of Japan Synthetic Rubber Co., Ltd.) was used. The number-average molecular weight, M_n, the heterogeneity index, M_w/M_n, and the weight fraction of polystyrene (PS), w_{PS}, were determined to be

---

* To whom correspondence should be addressed.

0024-9297/93/2226-0485$04.00/0

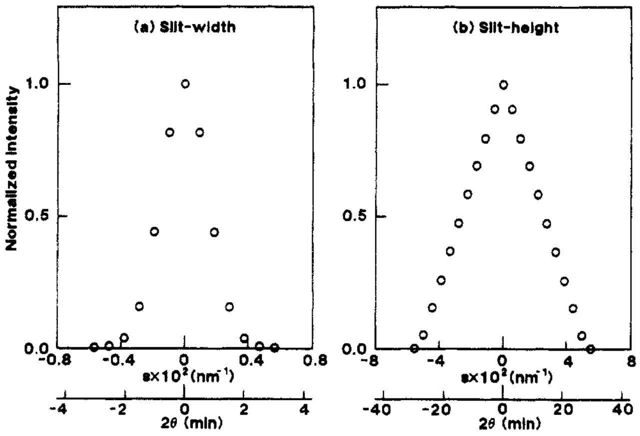

Figure 1. Slit-width (a) and slit-height (b) weighting functions of the incident beam on the detector plane.

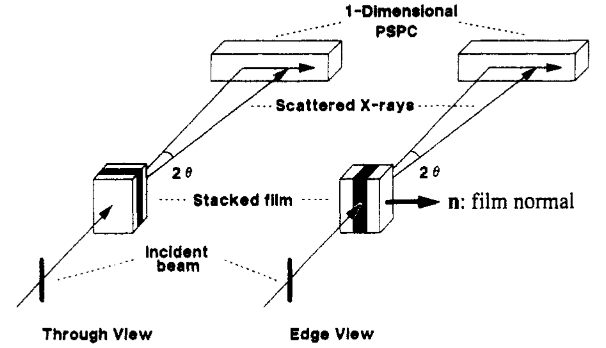

Figure 2. Schematic diagram showing the geometry of the experimental setting of SAXS.

6.31×10^4, 1.15, and 0.56 by membrane osmometry, GPC, and elemental analysis, respectively. The microstructure of polybutadiene (PB) blocks was determined by infrared spectroscopy (Morero method[25]) to be 33, 55, and 12 mol % for cis-1,4-, trans-1,4-, and 1,2-linkages, respectively. The film specimens were obtained by evaporating the solvent methyl ethyl ketone (MEK) from ca. 5 wt % polymer solution in MEK at room temperature. Since the solubility parameter values[26] are 8.1–8.6, 8.6–9.7, and 9.3 $[\mathrm{cal/cm^3}]^{1/2}$ for PB, PS, and MEK, respectively, MEK is a selectively good solvent for PS.

SAXS measurements were performed with an apparatus[27] consisting of a 12-kW rotating-anode X-ray generator, a graphite crystal for the incident beam monochromatization, a 1.5-m camera, and a one-dimensional position-sensitive proportional counter (PSPC). Cu Kα radiation with a wavelength, λ, of 0.154 nm was used. The incident beam with a line-shaped cross section was irradiated, and the scattered X-rays were collected with the one-dimensional PSPC which was horizontally set. The incident beam attenuated by a nickel filter[28] was directly measured by the PSPC to determine the weighting function of the optical system used in this work, and the result is shown in Figure 1. The geometry of our experimental setup of SAXS is schematically represented in Figure 2. The film normal is parallel to the propagation direction of the incident beam for the through view and parallel to the scanning direction of the PSPC for the edge view. The measured scattered intensities were further corrected for absorption due to the specimen, air scattering, thickness of the specimen, and thermal diffuse scattering arising from density fluctuations. The absolute scattered intensity was obtained by the nickel-foil method.[29]

A Hitachi H-600S electron microscope was used for the TEM of ultrathin sections of the specimens stained with osmium tetraoxide (OsO_4).

III. Results and Discussion

(A) Effects of Slit Smearing. Since the slit collimation with a finite slit height and a narrow slit breadth was used, the scattered intensity thus obtained as a function of scattering angle, which is called hereafter SAXS profile, is the smeared SAXS profile. Therefore, the smeared profile should be desmeared. However, the conventional method for desmearing of the profiles can be applied to an unoriented system but not for an oriented system.[30] Since the SAXS profiles for oriented systems are discussed in section III.B, we show first the effects of slit smearing on the SAXS profile.

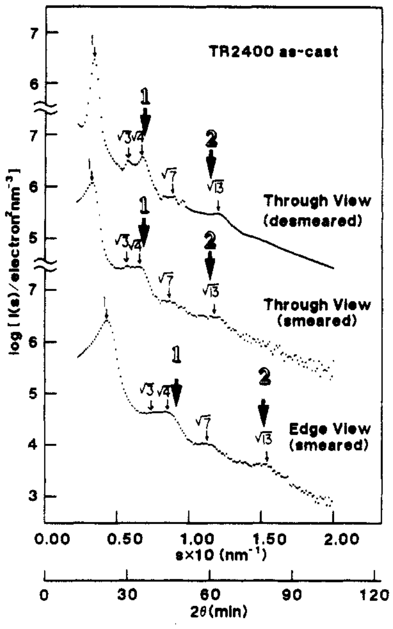

Figure 3. Semilogarithmic plots of the absolute scattered intensity $I(s)$ vs s, measured at room temperature for as-cast SBS specimens from a methyl ethyl ketone solution.

It is known that the cylindrical microdomains in the as-cast film have an orientation with their axes preferentially oriented parallel to the film surface. Therefore, the edge view gives the SAXS profile from oriented microdomains while the through view does the profile from unoriented microdomains. Hence, the slit correction (desmearing[28]) can be done only for the through view. In Figure 3, the smeared and desmeared profiles for through views of the as-cast specimen measured at room temperature are shown in a semilogarithmic plot of the absolute scattered intensity vs the magnitude of the scattering vector, s, which is given by

$$s = (2 \sin \theta)/\lambda \qquad (1)$$

with θ and λ being half the scattering angle and the wavelength of X-rays, respectively. The figure is utilized to show effects of the slit smearing on the profile. The width and intensity of each individual scattering peak are much affected by the slit smearing. On the other hand, the position of peak is not affected very much. Although the first-order peak shifts to a small s-region by the smearing effect, the amount of the shift is 1.6×10^{-3} nm^{-1} in s-value and is negligibly smaller than the difference between the position of the first-order peak for the as-cast specimen and that for the annealed specimen, which will be discussed later (see Figure 4 and section III.B). Therefore, in section III.B, we only focus on the peak position of the smeared SAXS profiles for edge view in the oriented systems in order to discuss the morphology transition.

(B) SAXS Results. In Figure 3 the smeared SAXS profile for edge view is also shown. Again the profile was measured at room temperature for the as-cast specimen. Several scattering peaks or shoulders were observed at relative s-values of 1, $3^{1/2}$, $4^{1/2}$, $7^{1/2}$, and $(13)^{1/2}$ in the

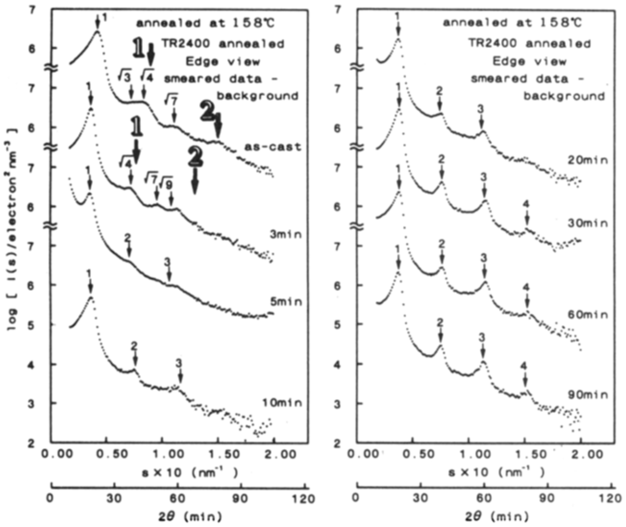

Figure 4. Semilogarithmic plots of the smeared absolute scattered intensity $I(s)$ vs s for the specimens annealed at 158 °C for edge view, measured at room temperature.

smeared profiles both for the through and edge views. These are diffraction peaks of hexagonally-packed cylindrical microdomains. Bragg spacing, d, was calculated with $d = 1/s_1$, where s_1 is the s-value of the first-order peak. The spacing was estimated to be 30.7 and 23.2 nm for through and edge views, respectively. This indicates an anisotropic packing of the cylindrical microdomains in the as-cast film. We will discuss this point later.

It is worthy of examining the SAXS profiles more closely. The peaks observed at s labeled by $(13)^{1/2}$ are more likely the scattering maxima arising from isolated cylindrical particles rather than the lattice peaks because of their spectral broadness. From the s-value of the particle scattering peaks, the average radius of the cylinders, R, is roughly estimated using the following condition for the particle scattering maxima of the isolated cylinders:[31]

$$2\pi s_i^{\mathrm{P}} R = 4.98, 8.364, 11.46, \ldots \quad \text{for } i = 1, 2, 3, \ldots \tag{2}$$

where s_i^{P} denotes the s-value of the ith-order particle scattering peak. If the scattering maxima at the positions labeled by the numerical numbers, i, with black thick arrows are assigned to ith-order particle scattering peaks ($i = 1, 2$), the calculated volume fractions, f, of the PB cylinders roughly agree with the molecular composition of TR2400. In the calculation of f, we assumed the perfectly hexagonal packing of the cylinders and f is given as

$$f = \frac{3^{1/2}}{2}\pi\left(\frac{R}{d}\right)^2 \tag{3}$$

The s_1^{P}-values 0.0681 nm^{-1} for both desmeared and smeared through views and 0.0903 nm^{-1} for the smeared edge view give 11.6 and 8.78 nm of the average radii of PB cylinders, respectively. The values of d were obtained to be 30.9 and 23.2 nm, respectively, for the through and edge views. Then f values were calculated to be 0.39 for both cases. This is roughly consistent with the volume fraction of PB-block chains ϕ_{PB} (=0.47) calculated from the molecular composition of $w_{\mathrm{PB}} = 0.44$.

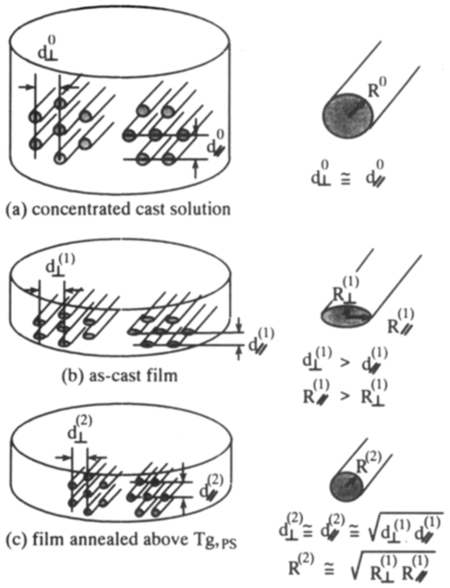

(a) concentrated cast solution

(b) as-cast film

(c) film annealed above $T_{g,\mathrm{PS}}$

Figure 5. Schematic representation of the hexagonally-packed cylinders with horizontally-stretched ellipsoidal cylinder cross sections formed in the as-cast film.

In Figure 4 the smeared SAXS profiles for the edge view are shown. These were measured at room temperature after annealing the specimens at 158 °C for 3, 5, 10, 20, 30, 60, and 90 min. For comparison, the profile of the as-cast film was included in the figure. A drastic change of the SAXS profiles is seen between the 3- and 5-min annealed specimens. The diffraction peaks from hexagonally-packed cylinders were observed for the 3-min annealed specimen. On the other hand, the relative positions of the scattering peaks for the specimens annealed for 5 min or longer can be assigned by integers, i.e., 1, 2, 3, ..., relevant to the diffraction peaks of the alternating lamellar microdomains. Thus, it was found that the morphology transition from cylindrical to lamellar microdomains occurred within 5 min upon annealing at 158 °C. Since the volume fraction of PS is 0.53, the lamellar morphology is thermodynamically stable at room temperature as well as at 158 °C. Therefore, this transition should be taken as that from the thermodynamically quasi-stable cylindrical morphology, which was formed via casting the block copolymer solutions with a selective solvent, to the stable lamellar morphology.[23]

Let us closely examine the change of the SAXS profiles with annealing time. The position of the first-order peak shifted toward a smaller s-region from 0.0431 to 0.0368 nm^{-1} within 3 min after annealing the as-cast film, but no more changed with further annealing. The Bragg spacing d-value for the 3-min annealed specimen is 27.2 nm. This peak shift can be explained as follows. During solvent evaporation, the cylindrical microdomains formed in the cast solution preferentially orient with their axes in a plane parallel to the film surface, as schematically shown in Figure 5a. The domain structure may be frozen-in when the PS-rich matrix phase is vitrified. Since the PS matrix still contains a certain amount of the solvent, volume contraction occurs during successive evaporation of the solvent. In this process the thickness of the cast solution decreases while keeping its area constant, which may lead to the cylinders having elliptical cross sections with their long axes oriented parallel to the film surface as shown in Figure 5b in the as-cast film. This process may also lead to a compression of the hexagonal lattice in the direction normal to the film surface as schematically shown in Figure 5b ($d_\parallel^{(1)} < d_\perp^{(1)}$). This is consistent with the SAXS for the as-cast film; that is, the spacing as observed for the through view ($d_\perp^{(1)} = 30.9$ nm) was larger than that for the edge view ($d_\parallel^{(1)} = 23.4$ nm). Asymmetric cross sections of the cylinders were also found by SAXS with $R_\parallel^{(1)} = 11.6$ nm and $R_\perp^{(1)} = 8.78$ nm where $R_\parallel^{(1)}$ and $R_\perp^{(1)}$ denote the radii of the cylinders in the directions parallel and normal to the free surface of the as-cast film, respectively. A similar asymmetric cross section was previously reported for the spherical microdomains formed in the solvent-cast film.[32] The asymmetric cross sections of the cylinders tend to become circular, the compressed lattices tend to recover normal hexagonal lattices, and hence its residual strain is relaxed when the as-cast film is annealed above T_g of PS. Actually the SAXS profiles of edge view showed the peak shifting toward a smaller s-region as a consequence of the increase of the spacing d in the direction normal to the film from $d_\parallel^{(1)}$ (=23.4 nm) to $d_\parallel^{(2)}$ (=27.2 nm). Here it was quite reasonable to observe the following relations for the Bragg spacings and the radii of the cylinders:

$$d_\perp^{(2)} \cong d_\parallel^{(2)} \cong [d_\perp^{(1)} d_\parallel^{(1)}]^{1/2} \quad \text{and} \quad R^{(2)} \cong [R_\perp^{(1)} R_\parallel^{(1)}]^{1/2} \qquad (4)$$

with $R^{(2)} = 10.3$ nm. For this specimen, $f = 0.39$ was obtained and again this is roughly consistent with the molecular composition.

It should be noted here that the positions of the scattering maxima located at the integer multiples of that of the first-order peak do not change upon annealing for times longer than 3 min and were therefore kept constant throughout the transition. The average value of d was 27.2 ± 0.5 nm. For the 5-, 10-, 20-, 30-, and 60-min annealed specimens, the scattering peaks became sharper with annealing time, while there is no significant difference between the profiles of 60- and 90-min annealed specimens. These observations indicate that cylinders are rapidly transformed into lamellae within 5 min, and then regularity of the alternating lamellae becomes higher upon further annealing in the time scale from 5 to 60 min.

(C) TEM Results. In order to confirm the morphological transition discussed in section III.B, the TEM investigation was conducted on ultrathin sections of the specimens stained with OsO_4. The observed microdomain structures for the as-cast and annealed specimens (annealed at 150 °C for 30, 60, and 120 min) are shown in Figures 6–9, where PB microdomains are selectively stained with OsO_4. The hexagonally-packed PB cylinders are dominantly seen for the as-cast specimen in Figure 6. Contrary to this, highly ordered alternating lamellae with uniform lamellar thickness are observed for the 120-min annealed specimen in Figure 9. Hence, the TEM observation definitely revealed the morphology transition.

Here let us closely examine the electron micrographs to elucidate the mechanism of the transition from cylinders to lamellae. In the 30-min annealed specimen (Figure 7) alternating lamellar microdomains are dominant. However, this morphology is much different from that of the 120-min annealed specimen (Figure 9). The characteristic features of the morphology for the 30-min annealed specimen are as follows: (1) Coherency of lamellar stacks is considerably low; i.e., their persistence lengths along their interfaces are considerably short or the interface is undulating, and the size of the stacks normal to the interfaces is also small. (2) There are still many regions in which cylinders exist, causing defects for the lamellar morphology. (3) There are regions showing probably the mesh morphology[33] in which the mesh layer composed of PB are stacked in the matrix of PS. In Figure 7 the hexagonally-packed cylinders are manifested in the circled region A, while the region in the circle B is seemingly showing the mesh morphology. The characteristic shape of the PB lamella with undulating interfaces or PB mesh is considered as a transient structure which may appear just after coalescence of cylinders. The cylinders which are as yet not transformed and the mesh morphology, both of which are the defects for the lamellar morphology, were still observed in the 60-min annealed specimen in Figure 8, the former defect being highlighted by the circled region A.

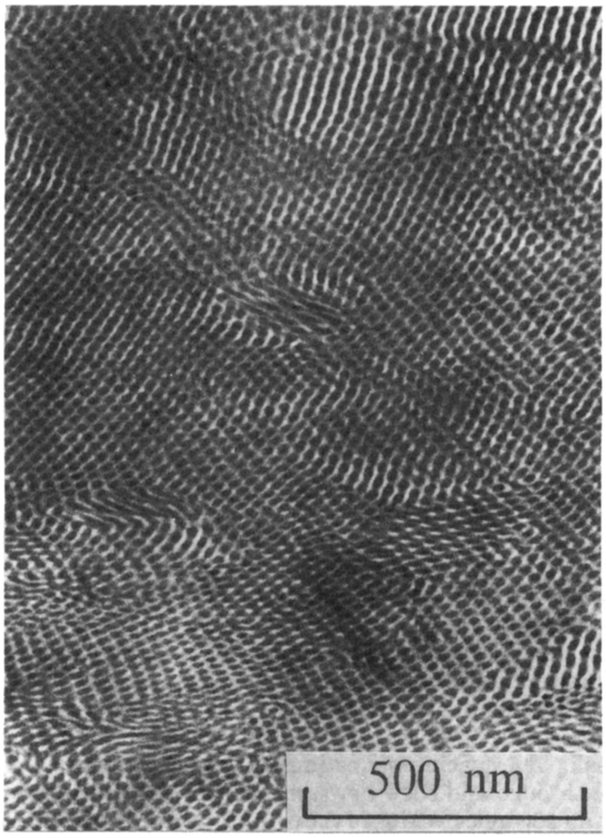

Figure 6. Electron micrograph of the as-cast specimen.

(D) Mechanism of Morphology Transition. On the basis of the SAXS and TEM observations, we present a schematic diagram in Figure 10 in which the morphology transition is viewed along the axis of the cylinders initially existing in the as-cast films. Parts a–d represent cylindrical morphology, a transient state from cylinders to lamellae, and lamellar morphology with low coherence and that with high coherence, respectively. The model view along the direction normal to the cylinder axis will be presented later in Figure 11. Parts a–d manifest the characteristic features of the morphology observed for the as-cast (more rigorously for the 3-min annealed specimen), 30-, 60-, and 120-min annealed specimens, respectively. In part b the cross section of each as-transformed cylinder is ellipsoidlike and neighboring cylinders tend to be interconnected as highlighted in region A in Figure 8, for example, where the original cylinder positions are indicated with thin circles. Such deformation of the cylinders results in decreasing mean curvature of the interface and hence in the relaxation of an excess bending free energy. The cylinders as yet not transformed in the original hexagonal lattice are highlighted in part c.

Since *no peak shift* was observed in the SAXS profiles throughout the morphology transition, it is not possible to consider that the transition is induced by collisions of the cylinders with their translational movements. The no peak shift also implies that *the spacing d of (100) plane in the cylinders turns into the interlamellar spacing D*, while conserving the condition of $d \cong D$. As revealed by SAXS and TEM, the transition from a to c is comparably fast. On the other hand, the process from c to d is slow. This is because a global change of the lamellar microdomains to increase coherence of lamellae should involve

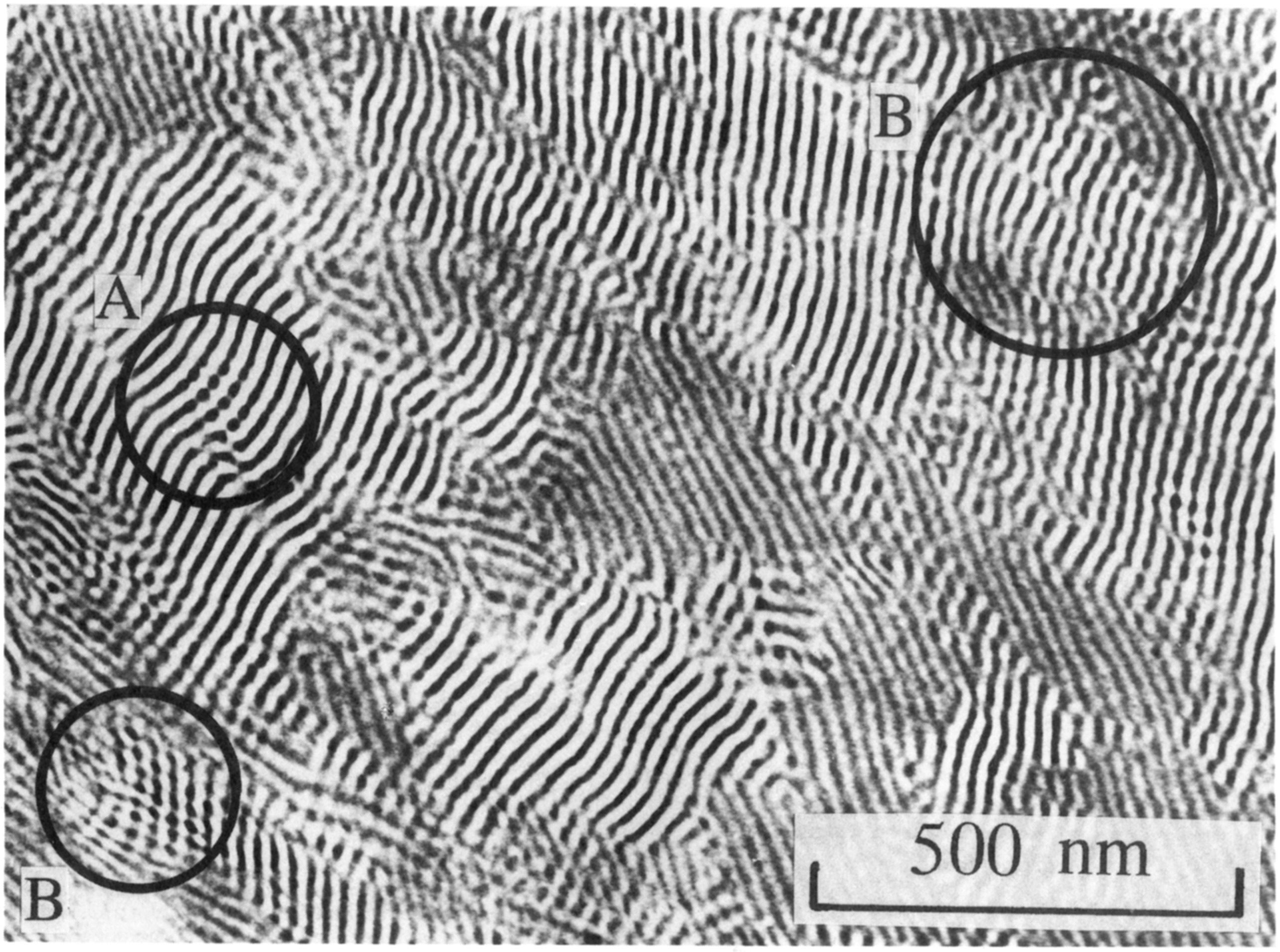

Figure 7. Electron micrograph of the 30-min annealed specimen (annealed at 150 °C).

a long-range cooperative ordering of lamellae or partial destruction-and-reformation of the undulating lamellae. Further investigation on the slow ordering process deserves future work.

Finally let us consider a possible scheme for the transition process without the translational movement of the cylinders. The scheme should involve coalescence of cylinders, as shown in Figure 11. The precursory step to the cylinder coalescence is the development of undulations along the length of the cylinders. For purely viscous systems this undulation is known as Tomotika's instability.[34] However, in our system the undulation is primarily driven by a change in the interface curvature, i.e., the curvature in the as-cast film becomes unstable at the annealing temperature, and the systems tend to achieve the new curvature equilibrium at this annealing temperature. Thus a primarily physical factor associated with this process may be elastic deformation of the block chains and interfaces, which is triggered by the relaxation of the unfavorable chain conformations for both PS and PB blocks in the quasi-stable morphology frozen in the as-cast film. When the SBS with ϕ_{PS} equal to 0.53 forms the cylindrical microdomains of the PB chains in the matrix of the PS chains under the condition of both chains satisfying the requirement for incompressibility, PS chains in the matrix are forced to expand and PB chains in the cylinders are forced to contract, causing convex curvature toward the center of the PB cylinders (see part 1 of Figure 11). This unfavorable conformation can be relaxed when the specimen is annealed above T_g of the glassy PS phase, which brings a change in the interface curvature and in the cross-sectional shape (part b of Figure 10) and hence instability and undulation of the interface in the as-cast films (see part 2 of Figure 11). The similar undulating interfaces were previously reported by Cohen et al.[24] for the morphology transition of cylinders pinching off into spheres. When the undulating interfaces accidentally approach each other and coalesce, channels can be formed between the adjacent cylinders (see part 3 of Figure 11). During stages 2 and 3 the average interface curvature starts to decrease. This reduction of the curvature continues through the transition process, decreasing the excess bending free energy encountered in the as-cast films. The channel grows in the direction along the axes of cylinders (see part 4 of Figure 11) in such a way that the cylinders are eventually transformed to lamellae, as shown by part 5 of Figure 11. The growth of the channel is similar to zippering. During stages 3 and 4, the PB meshes through which the PS channels traverse are formed as an intermediate structure. In this transition scheme presented in Figure 11 the translational movement of the cylinders is not necessarily considered. The interfacial thickness should be roughly kept constant throughout coalescence of cylinders because interfacial thickness is governed only by segmental interaction between PS and PB chains.

As revealed by SAXS and TEM observations, cylinders coalesced and were transformed into lamellae, while dissolution of the cylindrical microdomains was not observed prior to formation of the lamellar microdomains. This indicates that morphology transition does not necessarily require the entire dissolution of the domain structure. Let us consider this reason. Figure 12 schematically shows the change of the free energy involved in the morphology transition. Along with the transition path via the disordered state, the free energy barrier is considerably large due to the mixing of strongly repulsive

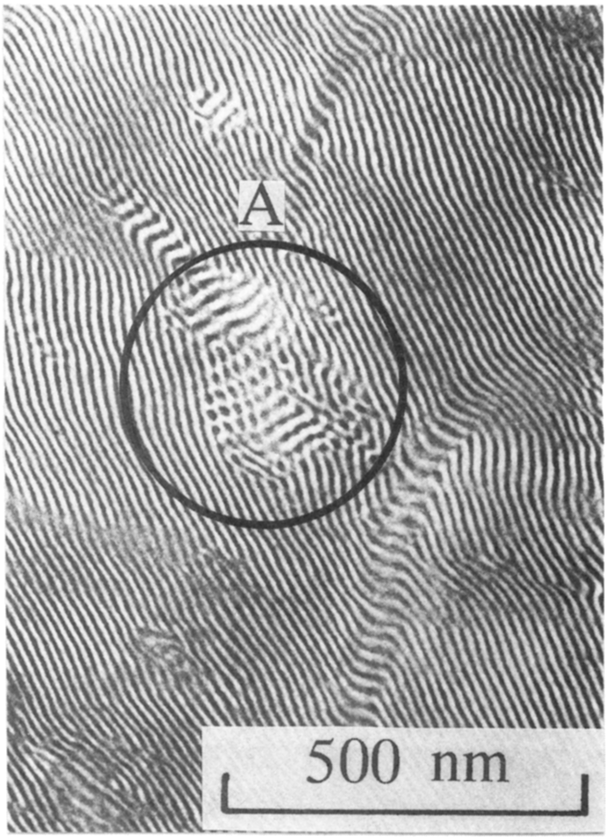

Figure 8. Electron micrograph of the 60-min annealed specimen (annealed at 150 °C).

Figure 9. Electron micrograph of the 120-min annealed specimen (annealed at 150 °C).

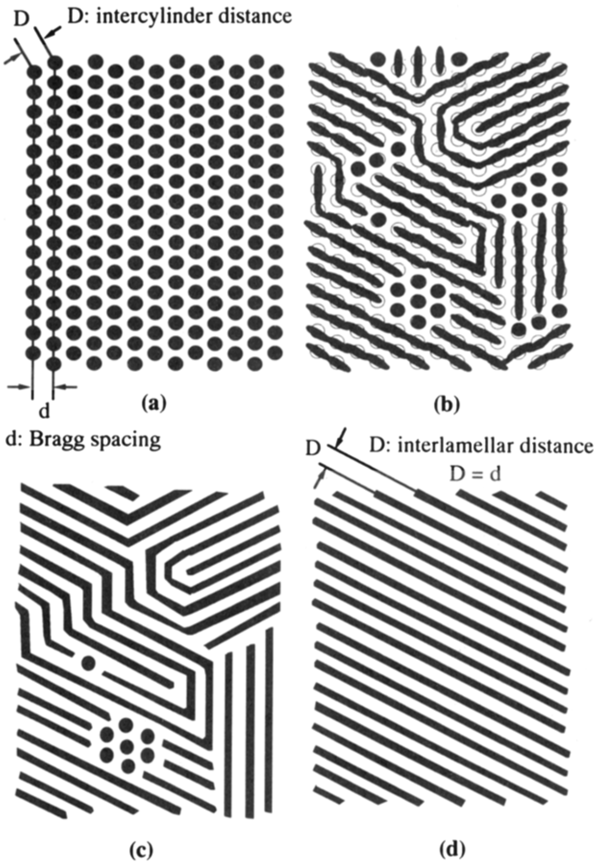

Figure 10. Two-dimensional projection for the change of structure. a–d represent cylindrical morphology, a transient state from cylinders to lamellae, and lamellar morphology with low coherence and that with high coherence, respectively, and correspond to the morphologies observed for the as-cast (more rigorously for the 3-min annealed specimen), 30-, 60-, and 120-min annealed specimens presented in Figures 7, 8 and 9, respectively.

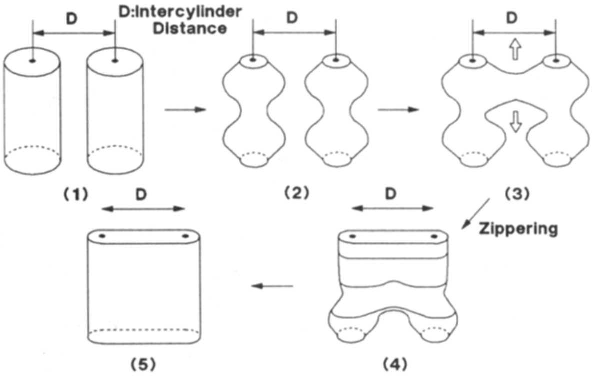

Figure 11. Scheme for morphological transition including coalescence of cylinders.

PS and PB block chains. On the other hand, the energy barrier for the coalescence scheme is expected to be rather small because it involves only the local disruption of the interface and local mixing of unlike segments as presented in Figure 11. Therefore, the transition scheme involving the coalescence of the cylinders may be more reasonable from the viewpoint of the lower energy barrier for the transition than the transition scheme involving the disordering.

IV. Concluding Remarks

In this study the morphology transition from cylinders to lamellae was studied complementarily by SAXS and TEM. It was found that the PB cylinders existing metastably in the solution-cast films were tranformed into thermodynamically stable lamellae on annealing at 150

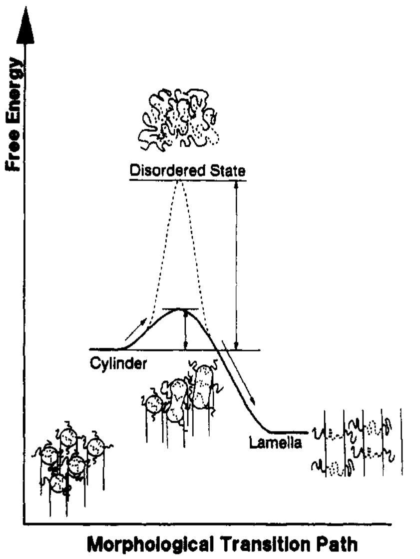

Figure 12. Schematic representation of the change of the free energy involved in the morphology transition.

°C. The transition turned out to occur via coalescence of cylinders without their translational movements of their center-of-mass. Movements of undulating interface induced by the instability of the interface, which in turn is caused by change of the interface curvature, might play an important role for the coalescence of the cylinders, and a scheme for the transition is presented in Figures 10 and 11. However, the present scheme is not deduced from the geometrical stability of the interfacial structures at the transient state. The orientation direction of the lamellae as transformed from the cylinders, i.e., whether the lamellar interface is formed parallel or perpendicular to the axes of the original cylinders, depends on the geometrical stability of the interfacial structure at the transient state.

It was also found by TEM that the coherency of lamellar microdomains thus formed became higher with prolongation of the annealing time; i.e., the persistence length of the undulating lamellae became longer. The waviness of the lamellae can be evaluated using paracrystal distortion factors g introduced by Hosemann[35] and d presented by Vonk.[36] In the next paper,[37] we will present an annealing time dependence of these distortion factors g and d as well as their annealing temperature dependence.

Acknowledgment. The authors are grateful to K. Kimishima for his help on the TEM experiments.

References and Notes

(1) Paul, D. R., Newman, S., Eds. *Polymer Blends*; Academic Press: New York, 1978.
(2) Legge, N. R., Holden, G., Schroeder, H. E., Eds. *Thermoplastic Elastomers*; Hanser: Munich, 1987.
(3) Molau, G. E. In *Block Polymers*; Aggarwal, S. L., Ed.; Plenum Press: New York, 1970.
(4) Hashimoto, T.; Todo, A.; Itoi, H.; Kawai, H. *Macromolecules* **1977**, *10*, 377.
(5) Hashimoto, T.; Shibayama, M.; Kawai, H. *Macromolecules* **1980**, *13*, 1237.
(6) Hashimoto, T.; Fujimura, M.; Kawai, H. *Macromolecules* **1980**, *13*, 1660.
(7) Hashimoto, T.; Shibayama, M.; Fujimura, M.; Kawai, H. In *Block Copolymers: Science and Technology*; Meier, D. J., Ed.; Gordon & Breach Science Publisher: Tokyo, 1983.
(8) Meier, D. J. *J. Polym. Sci.* **1969**, *C26*, 81.
(9) Meier, D. J. In *Block and Graft Copolymers*; Burke, J. J., Weiss, V., Eds.; Syracuse University Press: Syracuse, NY, 1973.
(10) Helfand, E. *Macromolecules* **1975**, *8*, 552.
(11) Helfand, E.; Wasserman, Z. R. *Macromolecules* **1976**, *9*, 879.
(12) Helfand, E.; Wasserman, Z. R. *Macromolecules* **1978**, *11*, 960.
(13) Helfand, E.; Wasserman, Z. R. *Macromolecules* **1980**, *13*, 994.
(14) Helfand, E.; Wasserman, Z. R. In *Developments in Block Copolymers*; Goodman, I., Ed.; Applied Science Publishers: Barking, U.K., 1984.
(15) Noolandi, J.; Hong, K. M. *Ferroelectrics* **1980**, *30*, 117.
(16) Hong, K. M.; Noolandi, J. *Macromolecules* **1981**, *14*, 727; **1983**, *16*, 1083.
(17) Whitmore, M. D.; Noolandi, J. *Macromolecules* **1985**, *18*, 2486; *J. Chem. Phys.* **1990**, *93*, 2946.
(18) Noolandi, J.; Hong, K. M. *Macromolecules* **1982**, *15*, 482.
(19) Leibler, L. *Macromolecules* **1980**, *13*, 1602.
(20) Ohta, T.; Kawasaki, K. *Macromolecules* **1986**, *19*, 2621.
(21) Fredrickson, G. H.; Helfand, E. *J. Chem. Phys.* **1987**, *87*, 697.
(22) Sakurai, S.; Hashimoto, T.; Fetters, L. J. *Polym. Prepr., Jpn., Soc. Polym. Sci., Jpn.* **1991**, *40* (3), 770. Sakurai, S.; Kawada, H.; Hashimoto, T.; Fetters, L. J., submitted to *Macromolecules*, *Proc. Japan Acad.*, **1993**, *69*, in press.
(23) Sakurai, S.; Hasegawa, H.; Hashimoto, T. *Polym. Prepr., Jpn., Soc. Polym. Sci., Jpn.* **1990**, *39* (3), 387. Sakurai, S.; Kawada, H.; Shiwaku, T.; Hashimoto, T., in preparation.
(24) Cohen, R. E.; Bates, F. S. *J. Polym. Sci., Polym. Phys. Ed.* **1980**, *18*, 2143.
(25) Morero, D.; Santambrigio, A.; Pori, L.; Ciampelli, E. *Chem. Ind. (Milan)* **1959**, *41*, 758.
(26) Grulke, E. A. In *Polymer Handbook*, 3rd ed.; Brandrup, J., Immergut, E. H., Eds.; Wiley: New York, 1989.
(27) Hashimoto, T.; Suehiro, S.; Shibayama, M.; Saijo, K.; Kawai, H. *Polym. J. (Tokyo)* **1981**, *13*, 501.
(28) Fujimura, M.; Hashimoto, T.; Kawai, H. *Mem. Fac. Eng., Kyoto Univ.* **1981**, *43* (2), 224.
(29) Hendricks, R. W. *J. Appl. Crystallogr.* **1972**, *5*, 315.
(30) Stein, R. S.; Wilkes, G. L. In *Structure and Properties of Oriented Polymers*; Ward, I. M., Ed.; Applied Science Publishers Ltd.: London, 1975; Chapter 3.
(31) Tanaka, H.; Hasegawa, H.; Hashimoto, T. *Macromolecules* **1991**, *24*, 240.
(32) Todo, A.; Uno, H.; Miyoshi, K.; Hashimoto, T.; Kawai, H. *Polym. Eng. Sci.* **1977**, *17*, 587.
(33) Hashimoto, T.; Koizumi, S.; Hasegawa, H.; Izumitani, T.; Hyde, S. *Macromolecules* **1992**, *25*, 1433.
(34) Tomotika, S. *Proc. R. Soc. London, Ser. A* **1935**, *150*, 322; **1936**, *153*, 302.
(35) Hosemann, R.; Bagchi, S. N. *Direct Analysis of Diffraction by Matter*; North-Holland: Amsterdam, The Netherlands, 1962.
(36) Vonk, C. G. *J. Appl. Crystallogr.* **1978**, *11*, 541. Baltá-Calleja, F. J.; Vonk, C. G. *X-ray Scattering of Synthetic Polymers*; Elsevier: Amsterdam, The Netherlands, 1989.
(37) Sakurai, S.; Taie, K.; Nomura, S.; Hashimoto, T., in preparation.